Electron capture in low-energy collisions of Sn^{3+} ions with H_2 and D_2

K. Bijlsma,[1,2] E. de Wit,[1,2] J. L. Pascual,[3] A. Kleinsmit,[1] E. Lalkens,[1] L. Assink,[1,2] M. Salverda,[1,2] L. Méndez,[4] O. O. Versolato,[2,5] I. Rabadán,[4] and R. Hoekstra[1,2]

[1]*Zernike Institute for Advanced Materials, University of Groningen, Nijenborgh 3, 9747 AG Groningen, The Netherlands*
[2]*Advanced Research Center for Nanolithography (ARCNL), Science Park 106, 1098 XG Amsterdam, The Netherlands*
[3]*Departamento de Química Física Aplicada, Universidad Autónoma de Madrid, Cantoblanco E-28049 Madrid, Spain*
[4]*Laboratorio Asociado al CIEMAT de Física Atómica y Molecular en Plasmas de Fusión, Departamento de Química, Universidad Autónoma de Madrid, Cantoblanco E-28049 Madrid, Spain*
[5]*Department of Physics and Astronomy and LaserLab, Vrije Universiteit Amsterdam, De Boelelaan 1100, 1081 HV Amsterdam, The Netherlands*

(Received 26 June 2025; accepted 10 September 2025; published 5 November 2025)

We report experimental single-electron-capture cross sections for Sn^{3+} ions impacting on H_2 and D_2 molecules at low projectile energies, ranging from 0.8 to 153 eV/u. The data were obtained in a crossed-beam-type experiment with a decelerated Sn^{3+} ion beam and a H_2 (D_2) gas target. Charge-state resolved Sn ion currents are measured with a retarding field analyzer. After an extensive description of the setup and measurement procedure, we present and discuss the results in comparison to model calculations. *Ab initio* calculations of potential energy curves, including spin-orbit interactions, are performed and used to fit a four-state diabatic model. The experimental and theoretical single-electron-capture cross sections show good agreement and are found to have values in the range of 20–45 $\times$ 10^{-16} cm^2 with a shallow maximum around 10 eV/u. We do not observe a significant difference between the cross sections for H_2 and D_2, as hinted at in our previous work at energies of 80–400 eV/u.

DOI: 10.1103/x84b-5kcn

I. INTRODUCTION

The atomic physics process in which a projectile ion colliding with a neutral atomic or molecular target takes one or more target electrons, known as electron capture or charge exchange, is relevant in several research areas, from fusion (e.g., Refs. [1–5]) to astrophysics (e.g., Refs. [6,7]) and lately also in nanolithography [8,9]. The particular collision system of Sn ions on H_2 molecules is highly relevant for the latest generation of nanolithography machines, which use 13.5-nm extreme ultraviolet (EUV) light for printing fine features on silicon wafers [10,11]. This light is emitted by highly charged Sn ions in a laser-produced plasma (LPP) of Sn [12,13] and subsequently collected and focused by the collector mirror, a large hemispherical Mo/Si-multilayer mirror. Fast Sn ions (KeV energy) coming from the LPP [14–17] have the potential to cause damage to this mirror by sputtering and implantation and therefore must be slowed and mitigated [18]. For this purpose, H_2 buffer gas has been chosen, primarily because of its low absorptivity of EUV light [19]. To find optimal buffer gas conditions, simulation models are used. Such models need fundamental atomic data for Sn ions that collide with H_2. Wu *et al.* [20] have measured the stopping power up to energies of several hundred eV. Later, stopping cross sections for energies up to several keV have been measured [21] and calculated [22]. The results of Abramenko *et al.* [21] indicate that the stopping cross section depends on the charge state of the Sn ion. Although Sn ions with charge states of 9+ to 15+ are responsible for EUV emission [12,13,23], energetic (>1 keV) ions emitted by the LPP have lower charge states of 3+ to 8+ [9,17,24], due to recombination in the peripheral part of the plasma [25]. While traveling through the buffer gas, electron capture in collisions of these ions with H_2 brings the charge state further down. Consequently, electron capture cross sections are needed for accurate simulation models for tin ion mitigation. According to the classical over-barrier model, the single-electron-capture cross section scales with the projectile's initial charge state q [26]. Electron capture cross sections for the higher charge states are therefore expected to be large, such that the lower charge states are dominantly present in the stopping gas. For that reason, we are mainly interested in the lower charge states.

Recently, in a first paper on single-electron capture in collisions of Sn^{3+} ions with H_2 and D_2 molecules [27], we presented experimental cross sections in the energy range of 76–430 eV/u (9–51 keV) and cross sections from semiclassical calculations in the energy range 10–1000 eV/u (1–120 keV). The experiments hinted at a significant energy dependence of the cross section for H_2, with the cross section growing larger at lower energies. For D_2, a less strong increase was observed, in better agreement with the semiclassical calculation. The observed behavior raises the question of whether the trends of an increasing cross section and a growing isotope effect continue at even lower energies. At

Published by the American Physical Society under the terms of the Creative Commons Attribution 4.0 International license. Further distribution of this work must maintain attribution to the author(s) and the published article's title, journal citation, and DOI.

9 keV (76 eV/u), however, we reached a lower energy limit set by inefficient ion beam extraction and transportation.

Electron capture by multiply charged ions of sub-keV energy colliding with neutral species is hard to study experimentally as highly charged ion sources (e.g., Ref. [28]) are operated at several kilovolts to produce the required intense beams of multiply charged ions. A way to achieve low relative velocities could be the technique of merged beams [29]. This technique has been successfully applied to systems in which neutral beams can be produced by electron detachment of negative ions, e.g., neutral atomic hydrogen produced by laser irradiation of H^- [30,31]. However, many atoms and molecules, including H_2, do not have negative ions and thus are not suitable for merged beam experiments. For H_2 as the target, to get to energies well below 1 keV/u, attempts in crossed-beam-type experiments were therefore made by means of putting the collision region on high voltage [32] or having the collision center inside an rf ion guide floating at high voltage [33]. However, to overcome issues with field penetration into the collision region and changing potentials in the collision chamber along the ion beam, affecting total charge-transfer measurements, we have put our whole crossed-beam apparatus on high voltage and used an electrostatic lens system for efficient deceleration and focusing of the decelerated ion beam. In this way, we were able to extend the measurements all the way down to 0.1 keV (0.8 eV/u).

A second upgrade on our experimental setup is the replacement of the Faraday cup by a retarding field analyzer (RFA), which provides charge state resolution in the measured ion beam current. The new apparatus is used to measure absolute cross sections for single- and bound double-electron capture (SC and BDC, respectively) from H_2 (and D_2) by Sn^{3+} ions, i.e., for the reactions

$$Sn^{3+} + H_2 \rightarrow Sn^{2+} + H_2^+, \quad (1)$$

$$Sn^{3+} + H_2 \rightarrow Sn^{+} + 2H^+. \quad (2)$$

Here, we focus on the results for single-electron capture. For double-electron capture, remarkably large cross sections were found at low energies. These results have recently been published in another work [34]. In the present work, we give an extensive description of how we obtained our experimental results for both processes.

On the theoretical side, in our previous work, spin-orbit effects were estimated using a simplified two-state model in which the single-capture channel was split into three components by applying the experimental spin-orbit splitting of the $Sn^{2+}(^3P^\circ)$ states uniformly at all internuclear distances. This approach allowed for a first-order estimate of the effect of spin-orbit coupling on the dynamics. In the present study, we improve upon that treatment by performing *ab initio* electronic structure calculations that explicitly include spin-orbit interactions, allowing us to construct accurate potential energy curves for the relevant electronic states. These results are used to guide the fitting of a four-state diabatic model that captures the asymptotic character of both the entrance channel and the dominant single-capture exit channel. The resulting model is then used in a full quantum (on projectile and electronic degrees of freedom) scattering calculation for both H_2 and D_2 as target molecules.

II. EXPERIMENTAL METHODS

A. Experimental setup

The experiments were performed in a crossed-beam setup in which a beam of Sn^{3+} ions crosses an effusive gas target of H_2. The setup is an upgrade of the setup used in our previous work [27]. The main differences are the use of decelerated Sn^{3+} beams to cover the low-energy regime below 9 keV and the use of a retarding field analyzer to determine the charge-state distribution of the Sn ions after crossing the H_2 target. Before discussing these two experimental upgrades, the ion beam facility will be recalled briefly.

The setup is a permanent station at the ZERNIKELEIF low-energy ion beam facility at the University of Groningen. Sn^{q+} ions are generated in a 14-GHz electron cyclotron resonance ion source (ECRIS), operated on a high potential V_{source}. Tin atoms are introduced into the ECRIS plasma by heating a crucible oven filled with solid pure tin. To stabilize the plasma, He gas is mixed in. After extraction from the ECRIS, the primary ion beam is mass-over-charge (m/q) selected using a 110° analyzing magnet with a resolution of about 0.5%, which allows for selecting a Sn ion beam of one specific isotope only. Although ^{120}Sn is the most abundant isotope of Sn, ions of the second-most-abundant isotope are used in the experiments, i.e., ^{118}Sn, because $^{120}Sn^{3+}$ has the same m/q ratio as Ar^+ and thus a possible (small) Ar^+ contamination cannot *a priori* be excluded for $^{120}Sn^{3+}$. The $^{118}Sn^{3+}$ ion beam is transported through a 10-m central beamline and steered into the crossed-beam setup by a 45° bending magnet. On the way from the bending magnet to the gas target, the ion beam is collimated by a set of six apertures, of which the smallest one has a diameter of 1.5 mm.

Primary Sn^{q+} ion beams can be extracted efficiently from the ECRIS with energies in the range of $3q$–$25q$ keV. The low-energy ion beams used in the experiments are generated by decelerating a primary Sn^{3+} ion beam of typically 21 keV just before it enters the collision chamber. To do so, the entire setup is floated on high voltage. A six-element deceleration lens is used to prevent ion losses due to beam broadening upon deceleration. More details about the deceleration process are given in Sec. II B.

The crossed-beam setup is schematically depicted in Fig. 1. At the center of the collision chamber, the ion beam traverses a jet of H_2 gas that is flowing from a capillary of 1.0 mm internal diameter that is situated 1.0 mm above the ion beam. A Bronkhorst FG-200CV high-precision mass flow controller is used to regulate the gas flow. Flowrates of 1, 2.5, and 4 mL/min are used in the experiments, which correspond to chamber pressures of (0.46, 1.14, and 1.81) $\times 10^{-4}$ mbar, respectively. The pressure in the chamber is measured by a Pfeiffer HPT 100 gauge. The background pressure in the chamber is $\approx 1 \times 10^{-8}$ mbar. During experiments, the base pressure is higher due to the presence of H_2 at $\approx 2 \times 10^{-7}$ mbar.

After traversing the gas target, the Sn ions are analyzed and collected by a RFA, which consists of a Faraday cup (FC) with four grids in front. A voltage can be applied to those grids, most notably a retarding voltage V_{ret} to the center two grids to create a well-defined potential barrier. Ions can only pass this barrier if the ratio E/q of their kinetic energy to

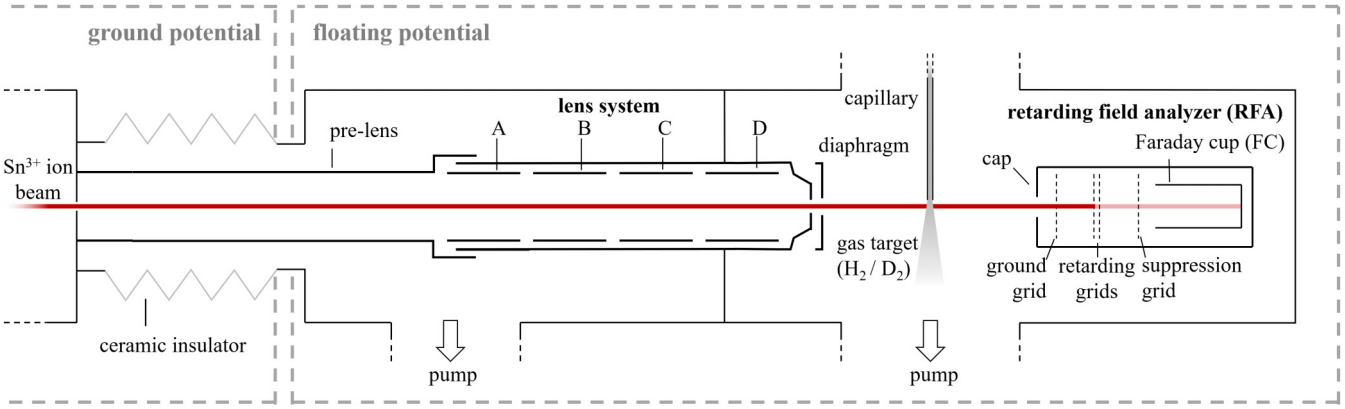

FIG. 1. Schematic of the crossed-beam setup. Dashed partial rectangles indicate the separation between the setup on a floating potential and the beamline on ground potential. Energy-, charge-, and mass-selected ions come in from the left, are gradually decelerated by the lens system, traverse the gas target created by a gas flow from the capillary, and are finally analyzed by the RFA. The six-element lens system consists of a prelens on ground potential, four equal-length cylindrical elements A–D to which variable voltages can be applied, and a final tapered element with a ϕ 1.5-mm exit diaphragm on setup potential. The RFA has four grids: a ground grid preventing field penetration into the collision region, two retarding grids to which a high voltage can be applied, thereby creating a homogeneous potential barrier to block ions based on their energy-to-charge ratio, and finally a negatively biased suppression grid preventing secondary electrons to escape the FC. The FC current, proportional to the number of ions and their charge state, is measured with a picoammeter. The background pressure in the chamber is $\approx 1 \times 10^{-8}$ mbar.

their charge state is larger than V_{ret}. The first grid is grounded to prevent field penetration from the retarding grids into the collision region. A suppressing voltage V_S of -100 V is applied to the final grid to prevent secondary electrons from escaping the FC. The FC current, which is proportional to the number of ions and their charge state, is read by a Keithley 6485 picoammeter. Our RFA is a modified four-grid Kimball FC73-A type of RFA. Wirings are altered such that it can be operated at higher voltages, up to 10 kV. The entrance of the RFA is covered with a so-called "cap," which has a 2.6-mm diaphragm.

B. Ion beam deceleration

For the primary ion beam to be decelerated, the experimental chamber, including all auxiliary equipment and electronics, is floated on a high potential. To eliminate the detrimental effect of ripples in high-voltage power supplies, this is accomplished by connecting the setup with the ECRIS and using an offset voltage V_{bias}, such that the setup potential equals $V_{\text{source}} - V_{\text{bias}}$. Consequently, the ion energy is reduced from qV_{source} to qV_{bias} (see Fig. 2). Additionally, a small intrinsic plasma potential V_{plasma} on the order of 10 V is common to an ECRIS ion source [35,36], and raises the ion beam energy by qV_{plasma}. The extra 30 eV for Sn^{3+} ions (0.25 eV/u) becomes considerable at the lowest energies and is therefore included in the energy values given in this paper.

Except for the case of very mild deceleration to energies still larger than 12 keV, the sudden step in potential causes strong beam divergence, which leads to large ion beam losses. To overcome this problem, an electrostatic deceleration and focusing lens system is used. The same lens system has been used previously by Bodewits *et al.* [35] and has a design based on similar designs that have been used successfully in the past [36,37]. The six-element lens system consists of a prelens on ground potential, four equal-length cylindrical elements A–D, and a final tapered element with a ϕ 1.5-mm exit diaphragm on setup potential (see Fig. 1).

The potentials on lens elements A–D were determined by an optimization process. The values were iteratively changed while reading the FC current I_{FC} as well as the current on the cap (including a current contribution from the ground grid) I_{cap}, with the goal of maximizing I_{FC} while having the ratio $I_{\text{FC}}/I_{\text{cap}}$ as large as possible, at least larger than unity. It was found optimal to use a potential scheme such that the ions undergo a brief acceleration in between two deceleration steps, as illustrated in Fig. 2. For the lowest energies, a gradual deceleration scheme was found to be optimal.

C. Measurement procedure

1. *Extracting single- and double-electron-capture cross sections*

In electron capture by Sn^{3+} from H_2, either one or both of the electrons of H_2 can be captured, reactions (1) (SC) and

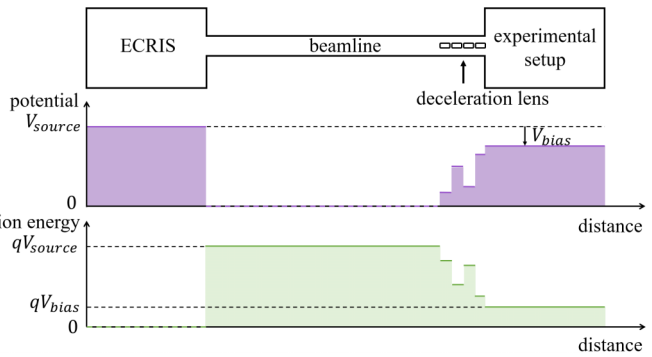

FIG. 2. Schematic illustrating the deceleration process. By connecting the setup to the ECRIS and using an offset voltage V_{bias}, the final ion energy is reduced from qV_{source} to qV_{bias}. In the deceleration lens, a typical potential configuration is illustrated, where ions undergo a brief acceleration in between two deceleration steps.

(2) (BDC), respectively. In the following derivation, we first assume to operate in the single-collision regime. A correction for double collisions is applied later, see Sec. II C 3.

The differential equation describing the number of Sn^{3+} particles, N^{3+}, as a function of distance z through the target gas is given by the following equation:

$$\frac{dN^{3+}}{dz} = -(\sigma_{32} + \sigma_{31})n(z)N^{3+}, \tag{3}$$

where $n(z)$ is the target number density and σ_{32} and σ_{31} are the SC and BDC cross sections, respectively. Let us now define the double-capture fraction f:

$$f = \frac{\sigma_{31}}{\sigma_{32}}. \tag{4}$$

Using this double-capture fraction, Eq. (3) can be solved for σ_{32}, yielding

$$\sigma_{32} = -\frac{\ln\left(N^{3+}/N_0^{3+}\right)}{(1+f)\int_0^L n(z)dz}, \tag{5}$$

where L is the length over which the ion beam overlaps with the gas target and N_0^{3+} is the initial number of Sn^{3+} ions. The RFA enables us to obtain the number of Sn^{1+}, Sn^{2+}, and Sn^{3+} particles, N^{1+}, N^{2+}, and N^{3+}, respectively (see Sec. II C 2). Conservation of particles dictates that $N_0^{3+} = N^{1+} + N^{2+} + N^{3+}$. Furthermore, in the single-collision regime, we can write

$$f = \frac{N^{1+}}{N^{2+}}. \tag{6}$$

The integral target density $\int_0^L n(z)dz$ is proportional to the pressure P in the collision chamber. The proportionality factor β is calibrated using O^{6+} ions, see Sec. II D. Equation (5) now becomes

$$\sigma_{32} = -\frac{\ln\left(\frac{N^{3+}}{N^{1+}+N^{2+}+N^{3+}}\right)}{\left(1+\frac{N^{1+}}{N^{2+}}\right)\beta P}. \tag{7}$$

The charge-state resolved ion numbers can be determined from the currents of singly, doubly, and triply charged Sn ions, which are measured with the RFA analyzer,

2. *Obtaining charge-state resolved Sn ion numbers*

After crossing the target, the ion beam arrives at the RFA and consists of Sn^{3+}, Sn^{2+}, and Sn^{1+} particles. The beam energy can be considered to be mone-energetic as the initial spread in ion energy due to the plasma potential of the ECRIS is on the order of 10 eV [38] and the energy transfer in capture collision is of a similar magnitude. Both uncertainties in final beam energy are small compared to our projectile energies, such that we can safely assume all ions arriving in the RFA to have approximately equal energy. Since the RFA selects on E/q, we can obtain charge-state resolution in the measured current by choosing appropriate retarding voltages.

To illustrate this, Fig. 3 shows the Faraday cup current as a function of retarding voltage for a 4-keV Sn^{3+} ion beam traversing the H_2 target at intermediate flow ($P_{\text{chamber}} = 1.14 \times 10^{-4}$ mbar). The red arrows indicate the voltages at which 3+, 2+, and 1+ particles of 4-keV energy are expected to be stopped by the RFA. Indeed, we see clear drops in the current at those voltages. Interestingly, after the 4-keV Sn^{1+} ions are blocked, a positive current remains visible until it drops to zero at around 4800 V. This is an artifact of the deceleration of the primary ion beam of 21 keV to 4 keV. Some hydrogen molecules diffuse out of the collision chamber into the deceleration lens and accumulate in the prelens, which is on ground potential. If a 21-keV Sn^{3+} ion undergoes single capture there, it results in a 21-keV Sn^{2+} ion. When this ion climbs 5.67 kV in potential in the deceleration process ($\frac{(21-4)\text{ keV}}{3e}$, as determined for a Sn^{3+} ion), it loses 11.33 keV of energy in this step and therefore has an energy of 9.67 keV in the collision chamber. A retarding voltage of 4.83 kV is needed to stop this particular ion. So Sn^{2+} (and possibly some Sn^{1+}) ions of a higher energy constitute the "artifact" ion current that is seen to remain as the 4-keV Sn^{1+} ions are stopped. We correct our analysis for this artifact.

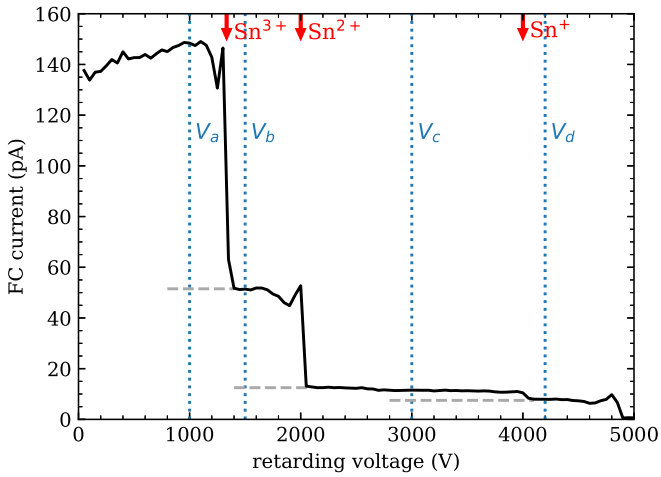

FIG. 3. The Faraday cup current as a function of retarding voltage for a 4-keV Sn^{3+} ion beam traversing the H_2 target at intermediate flow ($P_{\text{chamber}} = 1.14 \times 10^{-4}$ mbar). The ion beam is decelerated from a primary ion beam of 21 keV. Red arrows indicate the voltages at which 3+, 2+, and 1+ particles of 4-keV energy should be stopped by the RFA. Vertical dotted blue lines indicate typical retarding voltages used for determination of electron capture cross sections. Light-gray dashed lines are drawn at the approximate level of the current after a charge state is stopped, to indicate the "zero" levels for each of the three individual charge states.

In an actual measurement, we do not scan the retarding voltage as shown in Fig. 3, but instead we take current measurements at four carefully chosen voltages. The first voltage V_a is chosen to be below the voltage where the Sn^{3+} ions are expected to be blocked, see Fig. 3. The second voltage V_b is chosen beyond the voltage where the Sn^{3+} ions are blocked, but before the voltage where Sn^{2+} ions are blocked, and similarly the third voltage V_c is in between the voltages where the Sn^{2+} and Sn^{1+} ions are blocked. Finally, a measurement is performed at V_d, above the voltage where Sn^{1+} ions are blocked but before the next drop, to determine the artifact current. The three aforementioned currents are corrected for this artifact current by subtracting it from the currents measured at V_a, V_b, and V_c. A measured current I can be written as

$$I = e\sum_{q=1}^{3}(qN^{q+})/\Delta t, \tag{8}$$

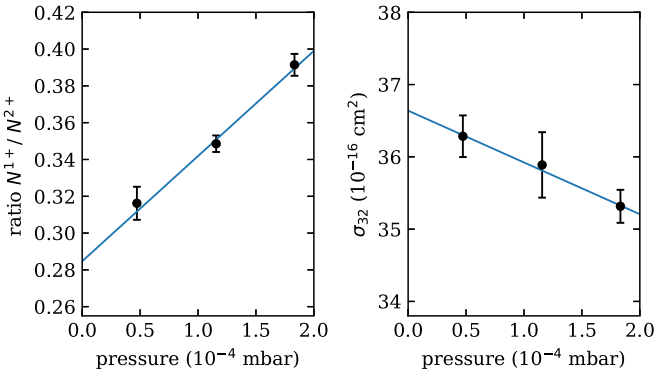

FIG. 4. Ratio N^{1+}/N^{2+} (left panel) and single-capture cross section (right panel) measured at three H_2 pressures for an incoming Sn^{3+} ion of 0.7 keV. Both panels show a linear fit through the data, taking data uncertainties into account. To eliminate the effect of double collisions, the value obtained by extrapolating the fit to zero pressure is taken as final value.

where e is the elementary charge, q the charge state of the Sn ion, N^{q+} the number of Sn ions with that charge state, and Δt the time interval over which the ions are measured. By taking differences of measured currents we can obtain N^{1+}, N^{2+}, and N^{3+}.

Returning to Fig. 3, it can be seen that as the retarding voltage increases from 0 to 1 kV, the FC current shows a gradual increase of about 10%. Then, as it nears the point where the Sn^{3+} ions are stopped, it shows an oscillation. This behavior can be attributed to an electrostatic lens effect in the RFA which is most prominent when the ions are slowed down to low velocity [39]. We correct our measurements for this voltage-dependent RFA transmission by performing a scan of the retarding voltage for the case when the H_2 gas flow is turned off such that the ion beam consists purely of Sn^{3+} ions. A five-point rolling average is applied to remove measurement noise. The resulting curve is used to determine transmission coefficients for the three charge states at the voltages V_a, V_b, and V_c. These coefficients are used to make corrections when transforming the currents into ion numbers. The effect of this correction is small, since ratios of currents (ion numbers) are used [see Eq. (7)]. Furthermore, the voltages V_a, V_b, V_c, and V_d are taken outside of the region where the curve shows oscillatory behavior.

3. Correction for double collisions

The expressions for f and σ_{32} [Eqs. (6) and (7), respectively] hold in the single-collision regime. Therefore, low gas flows are used so that only a small fraction of all Sn ions has undergone electron capture while traversing the gas target. However, even at these gas flows, a tiny fraction of all ions may undergo two consecutive charge transfer collisions. To correct for this effect, the measurements are performed at three different flows of H_2 gas and the results are extrapolated to zero pressure.

Figure 4 shows the situation and illustrates the procedure for a Sn^{3+} ion beam of 0.7 keV. The left panel shows the ratio N^{1+}/N^{2+} at three different pressures corresponding to the three gas flows that are used in the experiment. It clearly shows that the ratio increases at higher pressures. This can be explained by more double collisions happening at the higher target densities. The second collision turns a Sn^{2+} ion into a Sn^{1+} ion. The observed increase in the N^{1+}/N^{2+} ratio is with roughly 30% over our pressure range substantial and reveals a considerable single-electron-capture cross section for Sn^{2+} ions, in line with our earlier work on Sn^{2+} ions [40]. The value of the ratio obtained by extrapolating the fit to zero pressure is taken as the true fraction f of double-to-single capture fraction f (N^{1+}/N^{2+}) The right panel of Fig. 4 shows that the measured cross section indeed decreases linearly with pressure, but the effect is small (less than 3%). Nevertheless, here we also take the value obtained from extrapolating the fit to zero pressure as final value.

D. Calibration of the integral target density

The general expression for the single-capture cross section [Eq. (5)] contains the integral target density $\int_0^L n(z)dz$. The exact profile of the gas jet, and its overlap with the ion beam, is hard to determine accurately. Therefore, a different approach is used. An identical experiment is performed with a projectile with a known electron-capture cross section on H_2 such that the unknown integral target density can be determined. In fact, the proportionality factor β between the integral target density and the chamber pressure P is determined, such that the integral target density is obtained at any value of the gas flow.

In our previous study we used proton beams for cross-calibration. However, they are not suited for the present measurement procedure, which relies on measuring N^{q+}, $N^{(q-1)+}$, and $N^{(q-2)+}$ for a projectile of charge state q. We therefore need a projectile with $q \geqslant 3$ and for which single- and double-electron-capture cross sections are available. We have chosen the system O^{6+} on H_2 and used the cross section at 21 keV reported by Machacek *et al.* [41].

The complete experimental procedure, including correction for double collisions, has been repeated with O^{6+} projectiles. For the H_2 target, an undecelerated 21-keV O^{6+} beam was used, giving a β of $(75 \pm 3) \times 10^{16}$ cm^{-2} mbar^{-1}. However, for decelerated beams, the integral target density is expected to be somewhat smaller compared to when direct beams are used, because the gas that is present in the prelens contributes to the density for direct beams, whereas this part is excluded for decelerated beams (see Sec. II C 2). By using Sn^{3+} projectiles (and a fixed β), it was found that the cross sections measured with direct beams are (16 ± 5)% larger than with decelerated beams. In the actual measurements we always use decelerated beams. This means that the aforementioned β obtained with undecelerated O^{6+} should be scaled by the factor 1/1.16. In this way, a value for β of $(65 \pm 4) \times 10^{16}$ cm^{-2} mbar^{-1} for H_2 has been determined.

For the case of D_2 as target gas, β has been determined with a decelerated O^{6+} beam, resulting in a value of $(83 \pm 2) \times 10^{16}$ cm^{-2} mbar^{-1}.

E. Uncertainties

For each ion energy and gas flow, in a typical measurement cycle ten current samples are recorded at each of the four

voltages V_a, V_b, V_c, and V_d. From this data, four average currents are obtained which are subsequently converted to particle numbers as described in Sec. II C 2. These are used to calculate the f fraction and the single-capture cross section according to Eqs. (6) and (7), respectively. In total, four cycles are performed. If a plasma instability in the ECRIS causes a spike or dip in the current, that cycle is removed. An average and standard deviation for the two quantities of interest are then calculated over these cycles. For one energy, the above procedure is performed for three values of the gas flow. As described in Sec. II C 3, the final value is obtained from the y intercept of a linear fit made through the three data points, taking standard deviations into account. A (partial) statistical uncertainty Δ_f is quantified by the one-standard-deviation error on the fitted y intercept.

Other effects, e.g., the effect of temperature fluctuations, of mass flow controller and pressure gauge instabilities, and of beam focusing effects due to deceleration, are more difficult to quantify. Therefore, we repeated measurements at different days and looked at the repeatability of obtained cross sections. For the single-capture cross section a repeatability Δ_r of 5% was found.

The total statistical uncertainty Δ_S is obtained by taking the quadratic sum of Δ_f and Δ_r. This total statistical uncertainty defines the error bars presented in the figures shown in the Results section. Note that the uncertainty due to the calibration by the reference O^{6+} data is not included in the error bars, because it is a systematic uncertainty which could lead to a shift of all points, either up or down. This uncertainty has two contributions. First, the total uncertainty reported for the reference data is 3.4% [41]. Second, our experimental determination of β has an uncertainty of 6%. Combined, this leads to a systematic uncertainty of 7%.

III. THEORETICAL MODEL

A. *Ab initio* potential energy curves

To improve upon our previous work [27], the potential energy curves of the $(SnH_2)^{3+}$ system were obtained through calculations performed using an all-electron approach with a triple-zeta basis set of 96 atomic natural orbitals (ANO) for the valence electrons, including polarization functions. The contractions used were $(22s19p13d5f3g)/[7s6p4d2f1g]$ [42] for Sn and $(8s4p3d)/[3s2p1d]$ [43] for H.

Electronic wavefunctions were computed within the C_s point group. The vector $\mathbf{R}$ is defined as the displacement from Sn to the center of mass of H_2, and $\boldsymbol{\rho}$ as the internuclear separation vector of H_2. Throughout this work, the angle between $\mathbf{R}$ and $\boldsymbol{\rho}$ is fixed at 60°, which closely reproduces orientation-averaged results in similar systems [44,45].

The calculations followed a two-step approach, combining spin-orbit coupling with multireference methods. The first step employed the many-electron scalar relativistic second-order Douglas-Kroll-Hess (DKH) Hamiltonian [46,47]. Using this, state-averaged complete-active-space self-consistent-field (SA-CASSCF) [48] calculations were performed. The active space consisted of three electrons distributed among six molecular orbitals derived from the Sn 5s and 5p, and H 1s orbitals. The molecular orbitals were optimized separately

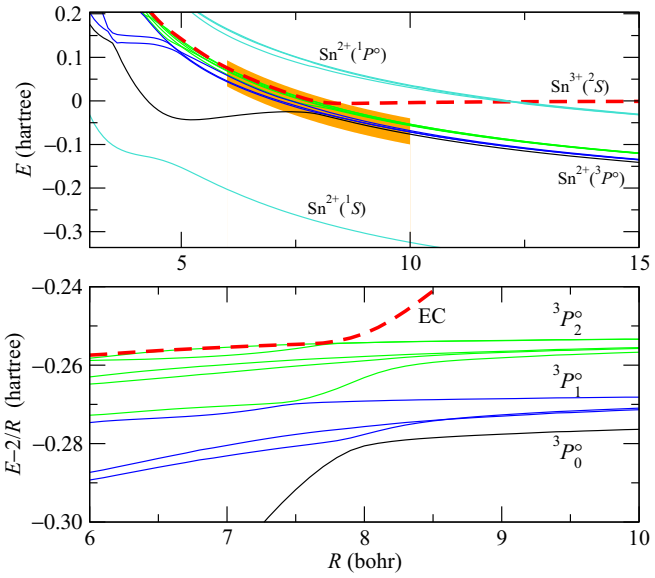

FIG. 5. Potential energy curves of the doublet states of the $(Sn + H_2)^{3+}$ system as functions of the distance between the Sn nucleus and the center of mass of H_2. In the top panel, we indicate the Sn ion charge and electronic state, while the bottom panel zooms in on the orange-shaded region of the top panel, subtracting a Coulomb repulsion term of $2/R$. The entrance channel (EC) is labeled, and single-capture states forming $Sn^{2+}(^3P_J^\circ)$ ions are indicated, where $J = 0, 1, 2$.

in SA-CASSCF calculations, considering the following electronic configurations of the relevant asymptotic channels:

$$Sn^{3+}(5s\ ^2S) + H_2(^1\Sigma_g^+), \tag{9}$$

$$Sn^{2+}(5s^2\ ^1S) + H_2^+(^2\Sigma_g^+), \tag{10}$$

$$Sn^{2+}(5s5p\ ^3P^\circ) + H_2^+(^2\Sigma_g^+), \tag{11}$$

$$Sn^{2+}(5s5p\ ^1P^\circ) + H_2^+(^2\Sigma_g^+). \tag{12}$$

State average over six $^2A'$ states, two $^4A'$ states, two $^2A''$ states, and one $^4A''$ state was considered and, to account for dynamic electron correlation, multistate second-order perturbation theory (MS-CASPT2) [49] calculations were performed, explicitly correlating the Sn 4s, 4p, 4d, and 5s and H 1s electrons. The standard IPEA shift value [50] of 0.25 a.u. was applied.

The second step is the incorporation of spin-orbit coupling effects using the atomic mean-field integral (AMFI) approximation [51] of the DKH spin-orbit coupling operator. To merge the spin-orbit interaction with the correlation calculations, the spin-free state shifting operator [52] was applied. For the incorporation of spin-orbit couplings computed with correlated wave functions and spin-orbit-free energies that include dynamic correlation, restricted-active-space state interaction spin-orbit (RASSI-SO) [53] calculations were performed using first-order perturbatively corrected wave functions and MS-CASPT2 energies. All states from the spin-free configurations were included.

Figure 5 presents the results of these multireference calculations of the potential energy curves for the spin-orbit

coupled electronic states of the $(SnH_2)^{3+}$ system. In the upper panel, the potential curves are shown as a function of the Sn–H_2 separation, with each curve labeled according to the electronic configuration of the tin ion, omitting the target molecule partner for clarity. The entrance channel, corresponding to $Sn^{3+}(^2S) + H_2(^1\Sigma_g^+)$, is depicted as a dashed line. Its crossing with the $Sn^{2+}(^1P^\circ) + H_2^+(^2\Sigma_g^+)$ channels is very narrow and has been diabatized. To highlight the most important interaction features, particularly the avoided crossings between the entrance channel (EC) and the single capture (SC) one leading to $Sn^{2+}(^3P^\circ) + H_2^+(^2\Sigma_g^+)$, the shaded orange region is expanded in the lower panel. In this zoomed-in view, a Coulomb term has been subtracted from the total energy to resolve the structure more clearly. At large internuclear separations, the curves converge toward the asymptotic limits associated with the three spin-orbit components of the $Sn^{2+}(5s5p\,^3P_J^\circ)$ multiplet, which are distinguished by color.

B. The diabatic model

Here, we focus on the electronic states relevant to the low-energy dynamics: the EC $Sn^{3+}(^2S) + H_2$ and the SC $Sn^{2+}(^3P^\circ) + H_2^+$, as illustrated in the lower panel of Fig. 5. The avoided crossing between these channels occurs near 8 bohr, a distance where the target is effectively quasi-isotropic. This leads to a quasi-C_s symmetry of the total system, which restricts significant couplings to occur primarily between states of the same spatial symmetry [54]. In this context, the entrance channel possesses A′ symmetry, and therefore only spin-orbit components of the $^3P_J^\circ$ manifold that also transform as A′ can couple efficiently to it. Specifically, two states of the $^3P_2^\circ$ multiplet, and one of the $^3P_1^\circ$, have A″ symmetry and are symmetry-forbidden from interacting with the entrance channel. These states can thus be excluded from the interaction model. Among the remaining components, those with quasi $m_J = 0$ character in each multiplet exhibit significant mixing with the entrance channel. Accordingly, we construct a diabatic model comprising four states: the entrance channel and one interacting SC component from each $^3P_J^\circ$ manifold ($J = 0, 1, 2$), where the superscript "°" indicates the odd parity of the electronic configuration.

The energy of the EC is modeled by a Morse potential to represent the molecular binding interaction between Sn^{3+} and the target molecule, with parameters $D_e = 0.042$ hartree, equilibrium distance $R_e = 5.23$ bohr, and exponential parameter $\alpha = 0.7$ bohr^{-1}.

The energies of the SC states are modeled using a short-range repulsive term combined with a long-range Coulomb potential characterized by an effective charge of $Q_{\rm eff} = 1.927e$, which reproduces the correct behavior at intermediate distances. An energy offset $\Delta E = 0.27$ hartree accounts for the difference between the EC and SC asymptotes, consistent with the *ab initio* results. The short-range repulsive exponential term, $105.0\exp(-3R^{0.85})$, was adjusted to replicate the curvature of the SC channels at short distances and to yield a diabatic potential that, after diagonalization, qualitatively matches the *ab initio* adiabatic curves.

Spin-orbit splittings were introduced to distinguish the $^3P_J^\circ$ components, using values $\Delta E(^3P_0^\circ - ^3P_1^\circ) = 0.0061$ hartree and $\Delta E(^3P_0^\circ - ^3P_2^\circ) = 0.021$ hartree, which closely match experimental values reported in Ref. [55] (0.0075 and 0.026 hartree, respectively).

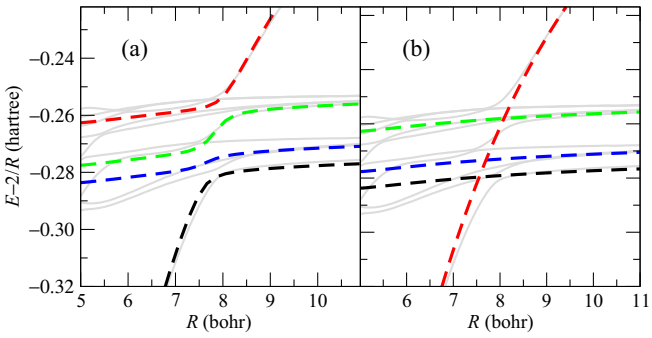

FIG. 6. The gray lines are the same as those shown in the bottom panel of Fig. 5. The thick dashed colored lines represent the adiabatic (a) and diabatic (b) curves of the four-state model defined in Eqs. (13)–(18).

The interaction terms between the EC and SC states were assigned a constant coupling value of 0.005 hartree. This magnitude is comparable to those employed in previous nonadiabatic scattering models [56], and was confirmed by fitting to reproduce the shape and position of the avoided crossings observed in the *ab initio* adiabatic potentials.

The resulting diabatic model Hamiltonian is defined as

$$H_{11}(R) = D_e\big(\{1.0 - \exp[-\alpha(R - R_e)]\}^2 - 1\big) \quad (13)$$

$$H_{22}(R) = Q_{\rm eff}/R - \Delta E + 105.0\exp(-3R^{0.85}) \quad (14)$$

$$H_{33}(R) = H_{22}(R) + \Delta E(^3P_0^\circ - ^3P_1^\circ) \quad (15)$$

$$H_{44}(R) = H_{22}(R) + \Delta E(^3P_0^\circ - ^3P_2^\circ) \quad (16)$$

with the off-diagonal couplings

$$H_{12} = H_{13} = H_{14} = 0.005 \quad (17)$$

$$H_{23} = H_{24} = H_{34} = 0. \quad (18)$$

To assess the validity of the proposed four-state diabatic model, we compare its potential energy curves with the *ab initio* results discussed previously. Figure 6 shows both the adiabatic states obtained by diagonalizing the model Hamiltonian (panel a) and the diabatic potentials used as input (panel b), overlaid on the *ab initio* curves from Fig. 5 (gray lines). The diabatic potentials are plotted as color-coded thick dashed lines for clarity: red for H_{11} (entrance channel), black for H_{22}, blue for H_{33}, and green for H_{44} (single-capture channels). The diabatic potentials [Fig. 6(b)] accurately reproduce the asymptotic behavior of the *ab initio* curves for $R > 8$ bohr, while the adiabatic energies [Fig. 6(a)] closely follow the *ab initio* adiabatic curves near the avoided crossing. Overall, the model captures both the correct asymptotic limits and a reasonably good description of the interaction region. The fact that a constant coupling between the entrance and single-capture channels suffices to reproduce the main features of the avoided crossing confirms the adequacy of the simplified diabatic approach.

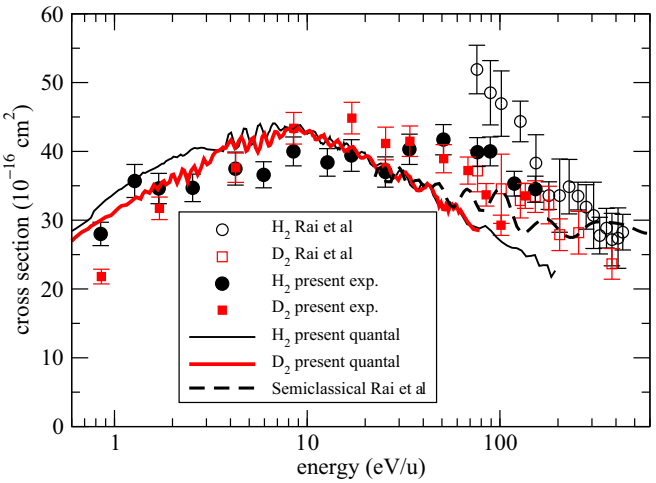

FIG. 7. Measured single-electron-capture cross sections for Sn^{3+} ions colliding with H_2 (solid black circles) and D_2 (solid red squares) as functions of projectile energy. Also shown are experimental results from Rai *et al.* [27] (open symbols), the semiclassical calculation from that work (dashed line), and the present quantum calculations for both H_2 and D_2 using the four-state model of Eqs. (13)–(18).

C. Quantal time-independent scattering

Scattering calculations were performed using a fully quantal formalism within the infinite-order sudden approximation (IOSA) [57], which is justified by the much shorter time ($\simeq 1.2 \times 10^{-14}$ s) a 10 eV/u Sn ion takes to traverse 10 bohr compared to the H_2 rotational period ($\simeq 2.8 \times 10^{-13}$ s). The multichannel log-derivative method [58], as detailed in Ref. [45], was employed with the diabatic Hamiltonian defined in Sec. III B.

Using standard collision theory, the scattering matrix elements S_j^l are obtained for each partial wave quantum number l. The total cross section for a transition from the EC to the final state j is given by

$$\sigma_j = \frac{\pi}{k^2} \sum_l (2l+1)|S_j^l|^2, \tag{19}$$

where k is the initial momentum.

IV. RESULTS AND DISCUSSION

Figure 7 shows the present experimental and theoretical results as well as the results from our previous work [27]. We first focus on the experimental results for H_2. The region of highest energies, around 100 eV/u, overlaps with the lowest energies of the previous measurements. The new data here do show an increasing trend toward lower energies; however, it is not as strong as suggested by the previous data. Going to lower energies, the cross section remains more or less constant till a decreasing trend sets in.

Following the previous measurements, we also performed the experiments with a D_2 target. It can be seen in Fig. 7 that the cross sections obtained for H_2 and for D_2 are very similar. Whereas the previous data showed an isotope effect around 100 eV/u, the current data do not exhibit a large effect anywhere over the full energy range from 1 to 200 eV/u.

The present D_2 data points show excellent agreement with the previous ones over the entire energy range of overlap. For H_2, the present data also align very well with the previous data in the energy range 150–430 eV/u, but, as stated above, do not support the remarkable increase exhibited by the data points below 150 eV/u by Rai *et al.* [27].

The previous detection method relied on measuring the difference in beam current with and without the gas target present and is therefore much more reliant on exact beam alignment to the Faraday cup. Beam broadening and scattering could have influenced the measurements in the case of a broad or off-centered ion beam. The previous lowest energies were also approaching the lower limit of the ion beam facility, which might have caused such ion beams. That means that a remarkably strong increase in cross section upon decreasing energy hinted at by the previous work is most likely an artifact of the measurement procedure.

Figure 7 compares the present theoretical single-capture cross sections for both H_2 and D_2, obtained using the four-state model, with experimental data. The quantum calculations show only minor differences between the H_2 and D_2 results across the explored energy range. The discrepancy with the semiclassical results of Ref. [27] arises from the exclusion, in the present model, of the channels $Sn^{2+}(^1S) + H_2^+(^2\Sigma_g^+)$ and $Sn^{2+}(^1P^\circ) + H_2^+(^2\Sigma_g^+)$, which were included in the semiclassical treatment.

Overall, the agreement between theory and experiment is good. The calculated cross sections are approximately 10% larger than the experimental values for energies below 10 eV/u. This discrepancy is attributed to the absence of the double capture (DC) channel in the present model, which becomes accessible only after the target has lost its first electron during the projectile's approach [34]. The DC process diverts about 35% of the population from the single-capture channel $Sn^{2+}(^3P^\circ) + H_2^+(^2\Sigma_g^+)$, but is only operative at short projectile-target separations ($R < 6.5$ bohr). In contrast, the dominant single-capture transitions occur at larger distances, between 6 and 9 bohr.

Had we estimated the interaction terms in Eq. (17) using the expressions given in Ref. [56], the resulting values would be $H_{12} = 0.0030$, $H_{13} = 0.0050$, and $H_{14} = 0.0054$. While not shown in Fig. 7, cross sections computed with these values yield similar magnitudes to those obtained with our fitted model around $E = 7$ eV/u. However, the energy dependence differs significantly: the Kimura-based couplings produce a flatter behavior at low energies and a more rapid decline at higher energies, deviating from experimental observations.

In Fig. 8, we present a detailed analysis of the contributions from each subchannel. The component with $J = 1$ remains nearly constant with energy, contributing around 30% across the full energy range. In contrast, the $J = 0$ and $J = 2$ components show complementary energy dependence: the $J = 2$ contribution decreases from 60% to 40% as the energy increases from 0.6 to 200 eV/u, while the $J = 0$ contribution increases from 10% to 30% over the same interval.

V. CONCLUSIONS

We extended previous measurements of single-electron capture in $Sn^{3+} + H_2$ and D_2 collisions down to

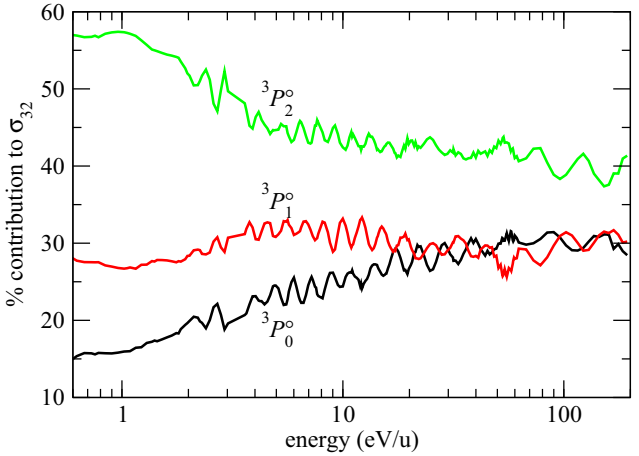

FIG. 8. Calculated contributions (in %) of the three $^3P^\circ_J$ channels to the total SC cross section for the $Sn^{3+} + H_2$ system. Results for $Sn^{3+} + D_2$ are very similar and therefore not shown separately.

unprecedentedly low energies of 0.8 eV/u by employing a decelerated ion beam in a floating-potential crossed-beam setup combined with a retarding field analyzer. This approach enabled precise charge-state-resolved detection of projectile products. The experimental results reveal a shallow maximum in the SC cross section around 10 eV/u and a decreasing trend at lower energies. Contrary to earlier findings, only a small isotope effect between H_2 and D_2 was observed over the full energy range of 1–200 eV/u.

The present experimental methodology enabled us to measure charge-state-resolved ion currents at very low projectile energies with excellent sensitivity and accuracy. A robust analysis procedure, including corrections for multiple collisions and instrumental effects, allowed for the reliable determination of absolute cross sections. The implementation of a retarding field analyzer proved critical for distinguishing single- and double-capture channels and for quantifying their respective cross sections. This approach demonstrated a high level of reproducibility and provided improved consistency over previous Faraday cup–based methods.

From the theoretical side, we have presented a comprehensive study of electron capture in low-energy collisions of Sn^{3+} ions with H_2 and D_2, incorporating spin-orbit coupling and multireference electronic structure calculations. Using a four-state diabatic model, we have successfully described the single-electron-capture dynamics. Scattering calculations within the infinite-order sudden approximation (IOSA) yielded cross sections in good agreement with experimental measurements. Minor deviations, particularly at energies below 10 eV/u, are attributed to the onset of the double-electron-capture channel, which is not included in the present model.

Furthermore, the contributions of the $^3P^\circ_J$ spin-orbit states to the SC cross section were found to vary systematically with energy: the $J = 2$ component decreases, while the $J = 0$ contribution increases over the explored energy range, reflecting a redistribution of coupling strength among the accessible exit channels.

Overall, the combined experimental and theoretical analysis offers a consistent and detailed description of the charge exchange dynamics in the $Sn^{3+} + H_2/D_2$ system. These results contribute to improving current models of Sn ion behavior in low-energy collisions and are relevant for applications such as EUV nanolithography, where accurate charge-state control is essential.

ACKNOWLEDGMENTS

The experimental work was carried out at the ZERNIKELEIF facility in the Zernike Institute for Advanced Materials of the University of Groningen as part of the research portfolio of the Advanced Research Center for Nanolithography (ARCNL), a public-private partnership between the University of Amsterdam, the Vrije Universiteit Amsterdam, the University of Groningen, the Netherlands organization for Scientific Research (NWO), and the semiconductor equipment manufacturer ASML. The computational support by the Centro de Computación Científica of UAM is also acknowledged.

DATA AVAILABILITY

The data that support the findings of this article are not publicly available upon publication because it is not technically feasible and/or the cost of preparing, depositing, and hosting the data would be prohibitive within the terms of this research project. The data are available from the authors upon reasonable request.

[1] H. Weisen, M. von Hellermann, A. Boileau, L. D. Horton, W. Mandl, and H. P. Summers, Nucl. Fusion **29**, 2187 (1989).
[2] R. C. Isler, Plasma Phys. Controlled Fusion **36**, 171 (1994).
[3] R. Hoekstra, H. Anderson, F. W. Bliek, M. von Hellermann, C. F. Maggi, R. E. Olson, and H. P. Summers, Plasma Phys. Controlled Fusion **40**, 1541 (1998).
[4] M. Reich, E. Wolfrum, J. Schweinzer, H. Ehmler, L. Horton, J. Neuhauser, and A. U. Team, Plasma Phys. Controlled Fusion **46**, 797 (2004).
[5] O. P. Ford, L. Vanó, J. A. Alonso, J. Baldzuhn, M. N. A. Beurskens, C. Biedermann, S. A. Bozhenkov, G. Fuchert, B. Geiger, D. Hartmann, R. J. E. Jaspers, A. Kappatou, A. Langenberg, S. A. Lazerson, R. M. McDermott, P. McNeely, T. W. C. Neelis, N. A. Pablant, E. Pasch, N. Rust *et al.*, Rev. Sci. Instrum. **91**, 023507 (2020).
[6] T. E. Cravens, Geophys. Res. Lett. **24**, 105 (1997).
[7] D. Bodewits, R. Hoekstra, B. Seredyuk, R. W. McCullough, G. H. Jones, and A. G. G. M. Tielens, Astrophys. J. **642**, 593 (2006).
[8] O. O. Versolato, Plasma Sources Sci. Technol. **28**, 083001 (2019).
[9] S. Rai, K. I. Bijlsma, L. Poirier, E. de Wit, L. Assink, A. Lassise, I. Rabadán, L. Méndez, J. Sheil, O. O. Versolato, and R. Hoekstra, Plasma Sources Sci. Technol. **32**, 035006 (2023).

[10] V. Y. Banine, K. N. Koshelev, and G. H. P. M. Swinkels, J. Phys. D: Appl. Phys. **44**, 253001 (2011).

[11] *EUV Lithography,* 2nd ed., edited by V. Bakshi (SPIE Press, Bellingham, 2018).

[12] G. O'Sullivan, B. Li, R. D'Arcy, P. Dunne, P. Hayden, D. Kilbane, T. McCormack, H. Ohashi, F. O'Reilly, P. Sheridan, E. Sokell, C. Suzuki, and T. Higashiguchi, J. Phys. B: At. Mol. Opt. Phys. **48**, 144025 (2015).

[13] F. Torretti, J. Sheil, R. Schupp, M. M. Basko, M. Bayraktar, R. A. Meijer, S. Witte, W. Ubachs, R. Hoekstra, O. O. Versolato, A. J. Neukirch, and J. Colgan, Nat. Commun. **11**, 2334 (2020).

[14] S. Fujioka, H. Nishimura, K. Nishihara, M. Murakami, Y.-G. Kang, Q. Gu, K. Nagai, T. Norimatsu, N. Miyanaga, Y. Izawa, K. Mima, Y. Shimada, A. Sunahara, and H. Furukawa, Appl. Phys. Lett. **87**, 241503 (2005).

[15] J. R. Freeman, S. S. Harilal, B. Verhoff, A. Hassanein, and B. Rice, Plasma Sources Sci. Technol. **21**, 055003 (2012).

[16] A. Bayerle, M. J. Deuzeman, S. van der Heijden, D. Kurilovich, T. de Faria Pinto, A. Stodolna, S. Witte, K. S. E. Eikema, W. Ubachs, R. Hoekstra, and O. O. Versolato, Plasma Sources Sci. Technol. **27**, 045001 (2018).

[17] L. Poirier, A. Lassise, Y. Mostafa, L. Behnke, N. Braaksma, L. Assink, R. Hoekstra, and O. O. Versolato, Appl. Phys. B **128**, 135 (2022).

[18] D. Nakamura, K. Tamaru, Y. Hashimoto, T. Okada, H. Tanaka, and A. Takahashi, J. Appl. Phys. **102**, 123310 (2007).

[19] I. Fomenkov, D. Brandt, A. Ershov, A. Schafgans, Y. Tao, G. Vaschenko, S. Rokitski, M. Kats, M. Vargas, M. Purvis, R. Rafac, B. La Fontaine, S. De Dea, A. LaForge, J. Stewart, S. Chang, M. Graham, D. Riggs, T. Taylor, M. Abraham *et al.*, Adv. Opt. Techn. **6**, 173 (2017).

[20] T. Wu, X. Wang, H. Lu, and P. Lu, J. Phys. D **45**, 475203 (2012).

[21] D. Abramenko, M. Spiridonov, P. Krainov, V. Krivtsun, D. Astakhov, V. Medvedev, M. van Kampen, D. Smeets, and K. Koshelev, Appl. Phys. Lett. **112**, 164102 (2018).

[22] N. Bartlett, A. Herschberg, J. Crouse, T. Dallal, J. Nuttal, J. Stahl, N. Braaksma, and D. Ruzic, Phys. Scr. **99**, 065411 (2024).

[23] J. Scheers, C. Shah, A. Ryabtsev, H. Bekker, F. Torretti, J. Sheil, D. A. Czapski, J. C. Berengut, W. Ubachs, J. R. Crespo López-Urrutia, R. Hoekstra, and O. O. Versolato, Phys. Rev. A **101**, 062511 (2020).

[24] J. Sheil, L. Poirier, A. C. Lassise, D. J. Hemminga, S. Schouwenaars, N. Braaksma, A. Frenzel, R. Hoekstra, and O. O. Versolato, Phys. Rev. Lett. **133**, 125101 (2024).

[25] R. A. Burdt, Y. Ueno, Y. Tao, S. Yuspeh, M. S. Tillack, and F. Najmabadi, Appl. Phys. Lett. **97**, 041502 (2010).

[26] A. Niehaus, J. Phys. B: At. Mol. Phys. **19**, 2925 (1986).

[27] S. Rai, K. I. Bijlsma, I. Rabadán, L. Méndez, P. A. J. Wolff, M. Salverda, O. O. Versolato, and R. Hoekstra, Phys. Rev. A **106**, 012804 (2022).

[28] R. Geller, Rev. Sci. Instrum. **69**, 1302 (1998).

[29] R. A. Phaneuf, C. C. Havener, G. H. Dunn, and A. Müller, Rep. Prog. Phys. **62**, 1143 (1999).

[30] B. van Zyl, N. Utterback, and R. Amme, Rev. Sci. Instr. **47**, 814 (1976).

[31] C. C. Havener, M. S. Huq, H. F. Krause, P. A. Schultz, and R. A. Phaneuf, Phys. Rev. A **39**, 1725 (1989).

[32] R. Hoekstra, J. P. M. Beijers, A. R. Schlatmann, R. Morgenstern, and F. J. de Heer, Phys. Rev. A **41**, 4800 (1990).

[33] G. Lubinski, Z. Juhász, R. Morgenstern, and R. Hoekstra, Phys. Rev. Lett. **86**, 616 (2001).

[34] L. Oltra, L. Méndez, I. Rabadán, K. Bijlsma, E. de Wit, and R. Hoekstra, Phys. Rev. Lett. **134**, 093002 (2025).

[35] E. Bodewits, H. Bekker, A. de Nijs, R. Hoekstra, D. Winklehner, B. Daniel, G. Kowarik, K. Dobes, and F. Aumayr, Nucl. Instrum. Methods Phys. Res., Sect. B **269**, 1203 (2011).

[36] S. T. de Zwart, A. G. Drentje, A. L. Boers, and R. Morgenstern, Surf. Sci. **217**, 298 (1989).

[37] J. Rajput, A. Roy, D. Kanjilal, R. Ahuja, and C. P. Safvan, Rev. Sci. Instrum. **81**, 043301 (2010).

[38] G. Lubinski, Z. Juhász, R. Morgenstern, and R. Hoekstra, J. Phys. B: At. Mol. Opt. Phys. **33**, 5275 (2000).

[39] Y. Sakai and I. Katsumata, Jpn. J. Appl. Phys. **24**, 337 (1985).

[40] K. Bijlsma, L. Oltra, E. D. Wit, L. Assink, I. Rabadán, L. Méndez, and R. Hoekstra, Atoms **12**, 9 (2024).

[41] J. R. Machacek, D. P. Mahapatra, D. R. Schultz, Yu. Ralchenko, A. Chutjian, J. Simcic, and R. J. Mawhorter, Phys. Rev. A **90**, 052708 (2014).

[42] B. O. Roos, R. Lindh, P. Malmqvist, V. Veryazov, and P. Widmark, J. Phys. Chem. A **108**, 2851 (2004).

[43] P. Widmark, P. Malmqvist, and B. O. Roos, Theor. Chim. Acta **77**, 291 (1990).

[44] L. F. Errea, A. Maciás', L. Méndez, I. Rabadán, and A. Riera, Int. J. Mol. Sci. **3**, 142 (2002).

[45] L. F. Errea, L. Fernández, L. Méndez, B. Pons, I. Rabadán, and A. Riera, Phys. Rev. A **75**, 032703 (2007).

[46] M. Douglas and N. M. Kroll, Ann. Phys. **82**, 89 (1974).

[47] B. A. Hess, Phys. Rev. A **33**, 3742 (1986).

[48] P. E. M. Siegbahn, J. Almlöf, A. Heiberg, and B. O. Roos, J. Chem. Phys. **74**, 2384 (1981).

[49] J. Finley, P. Malmqvist, B. O. Roos, and L. Serrano-Andrés, Chem. Phys. Lett. **288**, 299 (1998).

[50] G. Ghigo, B. O. Roos, and P. Malmqvist, Chem. Phys. Lett. **396**, 142 (2004).

[51] B. A. Heß, C. M. Marian, U. Wahlgren, and O. Gropen, Chem. Phys. Lett. **251**, 365 (1996).

[52] R. Llusar, M. Casarrubios, Z. Barandiarán, and L. Seijo, J. Chem. Phys. **105**, 5321 (1996).

[53] P. Malmqvist, B. O. Roos, and B. Schimmelpfennig, Chem. Phys. Lett. **357**, 230 (2002).

[54] W. Domcke, D. R. Yarkony, and H. Köppel, *Conical Intersections* (World Scientific, Singapore, 2004).

[55] K. Haris and A. Tauheed, Phys. Scr. **85**, 055301 (2012).

[56] M. Kimura, T. Iwai, Y. Kaneko, N. Kobayashi, A. Matsumoto, S. Ohtani, K. Okuno, S. Takagi, H. Tawara, and S. Tsurubuchi, J. Phys. Soc. Jpn. **53**, 2224 (1984).

[57] V. Sidis, *Advances in Atomic, Molecular, and Optical Physics* (Academic, New York, 1989), Vol. 26, pp. 161–208.

[58] B. Johnson, J. Comput. Phys. **13**, 445 (1973).